UC Davis

UC Davis Previously Published Works

Title

In Situ Solid-State Dewetting of Ag-Au-Pd Alloy: From Macro- to Nanoscale.

Permalink

https://escholarship.org/uc/item/7hq3h7dp

Journal

ACS Applied Materials & Interfaces, 16(45)

Authors

Lyu, Peifen

Matusalem, Filipe

Deniz, Ece

et al.

Publication Date

2024-11-13

DOI

10.1021/acsami.4c11397

Peer reviewed

Research Article

In Situ Solid-State Dewetting of Ag−Au−Pd Alloy: From Macro- to Nanoscale

Peifen Lyu, Filipe Matusalem, Ece Deniz, Alexandre Reily Rocha, and Marina S. Leite*

Cite This: ACS Appl. Mater. Interfaces 2024, 16, 62860−62870

Read Online

ACCESS | Metrics & More | Article Recommendations | SI Supporting Information

ABSTRACT: Metal alloy nanostructures represent a promising platform for next-generation nanophotonic devices, surpassing the limitations of pure metals by offering additional "buttons" for tailoring their optical properties by compositional variations. While alloyed nanoparticles hold great potential, their scalability and underexplored optical behavior still limit their application. Here, we establish a systematic approach to quantifying the unique optical behavior of the AgAuPd ternary system while providing a direct comparison with its pure constituent metals. Computationally, we analyze their electronic structure and uncover the transition of Pd d states to Pd/Ag hybridized s states in the bulk form, explaining the similar optical properties observed between Pd and AgAuPd. Experimentally, we fabricate pure metal and fully alloyed nanoparticles through solid-state dewetting, a scalable method. During the process, we trace the optical transition in the systems from the initial thin film stage to the final nanoparticle stage with in situ ellipsometry. We reveal the interplay between optical properties influenced by chemical interdiffusion and localized surface plasmon resonance arising from morphological changes with ex situ surface characterizations. Additionally, we analytically implement a metallic layer derived from the ternary system in a trilayer device, resulting in a single-time and irreversible color filter, to demonstrate an application encompassing a lithography-free and cost-effective route for nanophotonic devices.

KEYWORDS: Ag, Au, Pd, solid-state dewetting, nanoparticles, color filters, in situ ellipsometry, metasurfaces
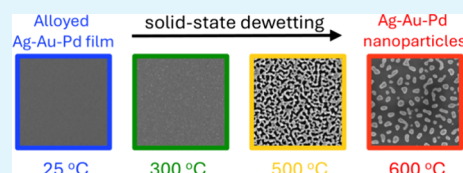
INTRODUCTION

Compared to their bulk counterparts, metal nanostructures exhibit superior optical performances attributed to their localized surface plasmon resonance (LSPR), arising from the confinement of the collective electric charge oscillations at the boundaries of the subwavelength structures.[1,2] Their tailorable geometric features have inspired the scientific community to explore the optical responses resulting from various geometries, sizes, and distributions.[3,4] Nevertheless, the predefined optical properties of pure metals continue to pose significant constraints for spectrum engineering, hindering the fulfillment of emergent needs in on-demand applications. Consequently, alloying two or more metallic elements present an effective pathway to modulate these functional properties, transcending the intrinsic limitations of individual constituents.[5−7] This engineered flexibility in dielectric functions promotes the utilization of alloyed metal nanostructures across a wide range of applications, such as electrocatalysts,[8,9] plasmon-enhanced catalysis,[10,11] photovoltaics,[12,13] chemical sensing,[14−17] and bioimaging[18] with improved functionalities.[19−22]

Traditionally, the fabrication of novel metal nanostructures has heavily relied on e-beam lithography (EBL). However, the high cost and limited efficiencies have impeded scalability and commercialization. Later, as one of the promising high-throughput nanofabrication methods, solid-state dewetting (SSD) emerged to make nanoparticles (NPs) from thin films

at appropriate annealing temperatures below their melting points. The SSD mechanism involves the introduction of thermal energy to the system, causing the materials in the initial continuous film far from their equilibrium state to agglomerate and develop into final nanostructures to minimize the total free energy through surface diffusion.[23] Temperature variations induce morphological changes in both monometallic and alloy systems, initiating an optical transition from light interference between metallic thin films to LSPR behavior excited by the final nanostructures.[24] Contrary to the high order and periodicity of the NPs created by conventional lithography processes, the nanostructures fabricated via SSD can be highly disordered in geometry and spatial distribution, offering pronounced strengths such as angle and polarization insensitivity, which are favorable for display applications.[25,26] Moreover, this lithography-free and single-step fabrication of metal NPs has been leveraged to realize practical applications, including structural color filters,[27] thermophotovoltaic with higher stability,[28,29] antifogging glasses,[30] and plasmon sensors.[31,32] While the majority of the field focuses on the

distinctive optical behaviors of metal NPs formed via SSD, limited attention has been given to the real-time changes in optical properties,[33,34] especially for alloy systems.

In this work, we present a framework for tuning the optical properties of metal NPs through nanostructuring and alloying, both offered by SSD. The ternary alloy system AgAuPd, recognized as a miscible solid solution,[35] is chosen for its superior performance in the field of catalysis[36] and chemical sensing,[37] compared to its elemental and binary counterparts. However, although its pure constituents have been extensively studied for nanophotonic applications, the optical behavior of the ternary alloy remains under-investigated. Starting with band structure calculations, we successfully identify the origins of characteristic optical properties in the AgAuPd bulk material, predominant in the infrared (IR) range. Subsequently, through a combination of in situ ellipsometry and ex situ surface characterizations, we experimentally demonstrate the real-time optical transitions as a direct consequence of both morphological and chemical composition changes traversing from the nanoscale thin film and ultimate NP stage, achieved through a scalable SSD process. Finally, the exceptional optical responses of the ternary alloy are showcased as the key for a one-time, irreversible color filter utilizing a lithography-free, cost-effective method.

■ RESULTS AND DISCUSSION

Electronic Structure of Bulk AgAuPd Alloy. Starting from understanding the origins of optical transitions within the bulk alloy, we employ density functional theory (DFT) calculations to first analyze its electronic structure. Our system comprises 27 atoms, with equal proportions of Ag, Au, and Pd, distributed in a $3 \times 3 \times 3$ fcc supercell (see Figure S1 and Table S1) following the special quasi-random structure (SQS) methodology.[38] The system is fully relaxed before the band structure calculations (see Experimental Section for complete details of the calculations). Figure 1 shows the band structure
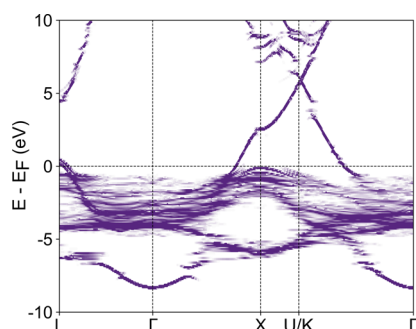

Figure 1. Density functional theory of AgAuPd alloy. Unfolded DFT band structure of the $Ag_{0.33}Au_{0.33}Pd_{0.33}$ alloy formed by a unit cell with 27 atoms in a fully relaxed configuration. The Fermi level is represented by the dashed line at an $E - E_F = 0$.

of the $Ag_{0.33}Au_{0.33}Pd_{0.33}$ alloy unfolded onto an irreducible fcc cell. Notably, minimal smearing of the band is observed for states above the Fermi energy level (E_F) around X, indicating that the electron bands of the disordered alloy largely retain the characteristics of a pure metal bulk system. Conversely, a smeared band of d character is evident from −5.0 eV up to E_F, signifying strong hybridization of d orbitals for each constituent.

To quantify the character of each band present in the dispersion relation, we compare the electronic band structures of the pure metals with those of the $Ag_{0.33}Au_{0.33}Pd_{0.33}$ alloy, projected onto each metal, see Figure 2. As previously reported, both Ag and Au display optical transitions in the visible and ultraviolet range at 3.65 and 2.1 eV, respectively.[39,40] However, bulk Pd presents a strong absorption contribution from the mid-infrared region due to the proximity of the d orbitals ($E - E_{Fermi} < 0$) to the Fermi level, evidenced by the interband transitions marked with the black arrows at the X point in Figure 2a–c.[39] For the alloy, we first notice that the electronic states of Au and Ag are strongly hybridized (Figure 2d,e). Most notably, the deeper d state in Au, lying between 7.5 and 10.0 eV below the Fermi energy for the pure metal situation, is shifted upward in energy, with almost indiscernible projected contributions from each atom. Moreover, a slightly stronger contribution from Ag, compared to Au, is noted in the low-lying states close to the Fermi level (between −2.5 and −5.0 eV) in Figure 2g. This observation aligns with previous findings in $Au_xAg_{(1−x)}$ binary alloys.[41] However, states from −2.5 eV up to the Fermi level are strongly dominated by the d orbitals of Pd (see Figure 2h,i), resembling the behavior observed in bulk Pd, suggesting a potential interband transition in the mid/far IR range of the electromagnetic spectrum. Concurrently, orbitals up to 10 eV above E_F primarily originate from Ag, with some secondary contributions from Pd. Thus, we anticipate that the overall absorption would be influenced by transitions from Pd d states to Pd/Ag hybridized s states.

Optical Properties of Thin Metal Film. While simulated electronic band structures provide insights into the underlying physics of the optical behavior in various bulk metal systems, we begin the experimental validation from the thin film to the nanoparticle stage. As depicted in Figure 3a, the initial as-deposited metal thin films are prepared by e-beam evaporation (EBE) onto a Si substrate with a thin native oxide layer (∼2.2 nm characterized by ellipsometer), while the trilayer metal stack is formed by sequentially depositing 5 nm of Ag, Au, and Pd. Thus, the thickness of the trilayer is approximately 15 nm (Table S2). Their dielectric functions ε_1 and ε_2, in Figure 3b,c, are determined by fitting the mutiangular spectroscopic ellipsometry (SE) measurements with the B-spline models (see Figure S3).[42] The optical properties of the pure metal thin film, Ag, Au, and Pd, are comparable with what were reported in the literature (see Figure S3e−g).[39,40] Both Ag and Au exhibit low optical absorption (ε_2) throughout the UV−vis−NIR (193−1680 nm) range, while Pd displays comparable absorption for wavelength <500 nm but greater loss at longer regime. In a ternary system, the interdiffusion of different metal atoms poses challenges to monometallic dewetting processes, governed by surface energy, surface diffusion, and activation energy.[43] Considering the magnitude of the surface energy of the three metals: Ag (1065 mJ/m^2) > Au (1363 mJ/m^2) > Pd (1808 mJ/m^2),[35,44] we expect easier interdiffusion between Ag and Au and greater difficulty at the Ag/Pd interface. Therefore, the trilayer thin film stack is deposited in the order of Ag, Au, and Pd from bottom to top to enhance the dewetting process. Here, the optical model for the trilayer metal stack is considered as one single layer rather than three separate layers consisting of individual metals for a more accurate description of the optical properties (see Figure S3d). This decision accounts for the deviation of dielectric functions of each ultrathin metal film from their respective bulk values due to
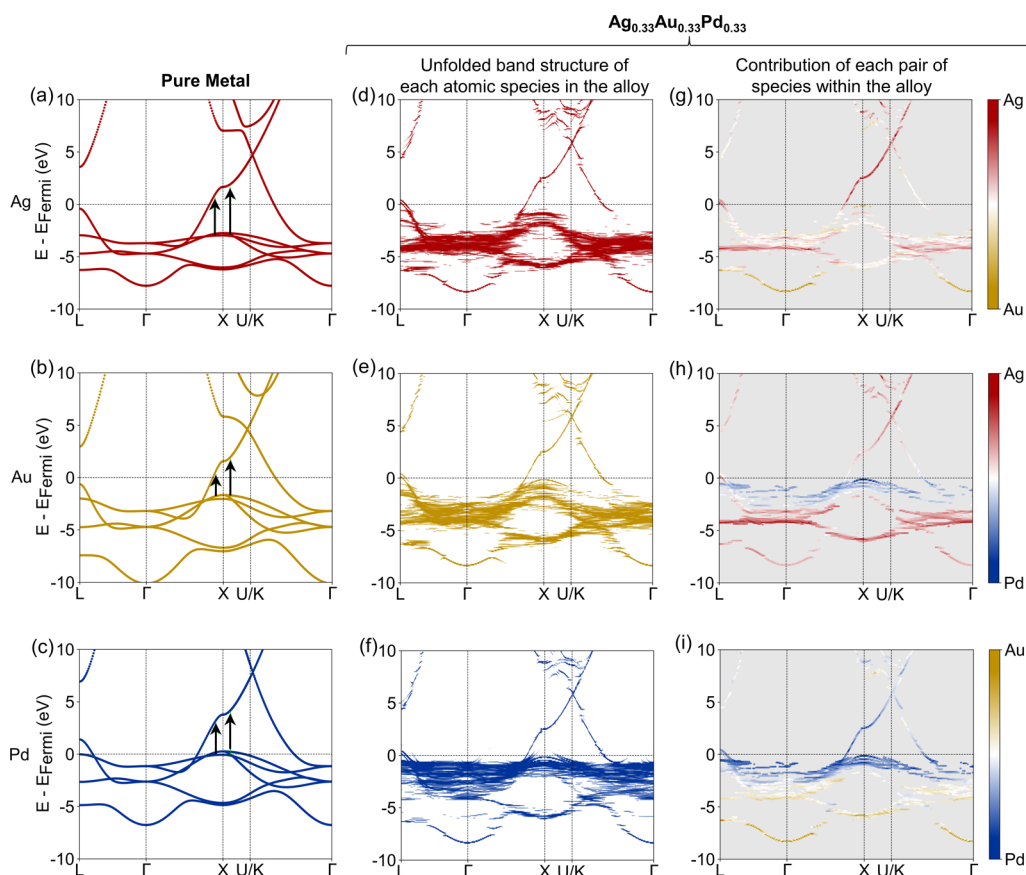
Figure 2. Band structure of pure metals and AgAuPd alloy. Density functional theory of bulk, pure (a) Ag, (b) Au, and (c) Pd. Unfolded DFT band structures of the $Ag_{0.33}Au_{0.33}Pd_{0.33}$ alloy projected onto each atomic species: (d) Ag, (e) Au, and (f) Pd. Contribution of each pair of species within the $Ag_{0.33}Au_{0.33}Pd_{0.33}$ alloy: (g) (Ag, Au), (h) (Ag, Pd), and (i) (Au, Pd). The color bars indicate the normalized level of contribution for each metal displayed, where white refers to equal contributions from each pair of metals within the alloy. The dashed line at $E - E_{Fermi} = 0$ represents the Fermi level. The black arrows represent the main interband transitions.
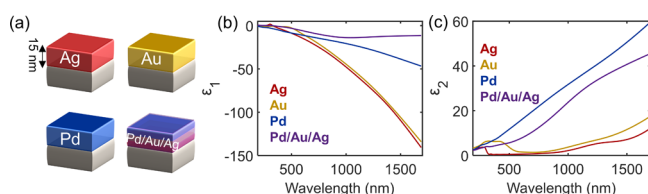

Figure 3. Optical properties of thin metal films. (a) Schematic of 15 nm metal thin films, Ag, Au, and Pd and trilayer Pd/Au/Ag (from top to bottom) on Si substrates. Corresponding dielectric functions (b) ε_1 and (c) ε_2 of 15 nm thin metal film as deposited (for the detailed fitting model, see Table S2 and Figure S3).

increased electron collision frequency.[45] Consequently, the dielectric functions of the Pd/Ag/Au stack have a greater similarity with Pd, the topmost layer in the stack, but are influenced by the presence of Ag and Au. These as-deposited thin film samples have relatively smooth and continuous surface with RMS < 1.1 nm and minimal substrate exposure, as verified by atomic force microscopy (AFM) and scanning electron microscopy (SEM) (Figure S4), excluding the possibility that the formation of final nanoparticles is a result of an initial nanostructured film. The observed grainy structures result from the connections between numerous nanoscale crystalline grains formed through the Volmer–Weber growth mechanism. During the deposition step, atoms diffuse across the substrate surface, initiating nucleation,

forming small islands, and ultimately coalescing into a thin film.[46] These pre-existing grain boundaries facilitate spontaneous void growth and edge retraction during thermal annealing, which drives further dewetting and leads to the formation of nanoparticles.[47,48]

In Situ Optical Behavior of Single Metal Thin Films. The next step is to turn thin metal films into nanoparticles following the SSD process, a highly scalable nanofabrication method. In addition to morphological changes, this process triggers optical transitions from normal light interference between the thin films to LSPR excited by the nanostructures. Therefore, to access the in situ optical behavior during this dynamic process, we have placed our thin metal film samples in a heating chamber equipped with a spectroscopic ellipsometer, heating up to 600 °C and holding for 1 hour (h), following the temperature profile in Figure S5. We select 600 °C as the maximum temperature for the SSD process after considering the thermal stability of the materials involved and our technical limitation (the maximum temperature of the heating stage for in situ ellipsometer is 600 °C). This temperature has been shown to be sufficient for both Ag and Au thin film (12−15 nm) to form well-defined nanoparticles via SSD,[24,49] where the nanostructures present clearly outlined edges and negligible coalescence, indicating that most of the surface diffusion process has occurred and that the nanoparticles are close to an equilibrium state. Further, it has been reported that 25 nm of Au−Ag−Pd trilayer nanodisk attained by templated deposition
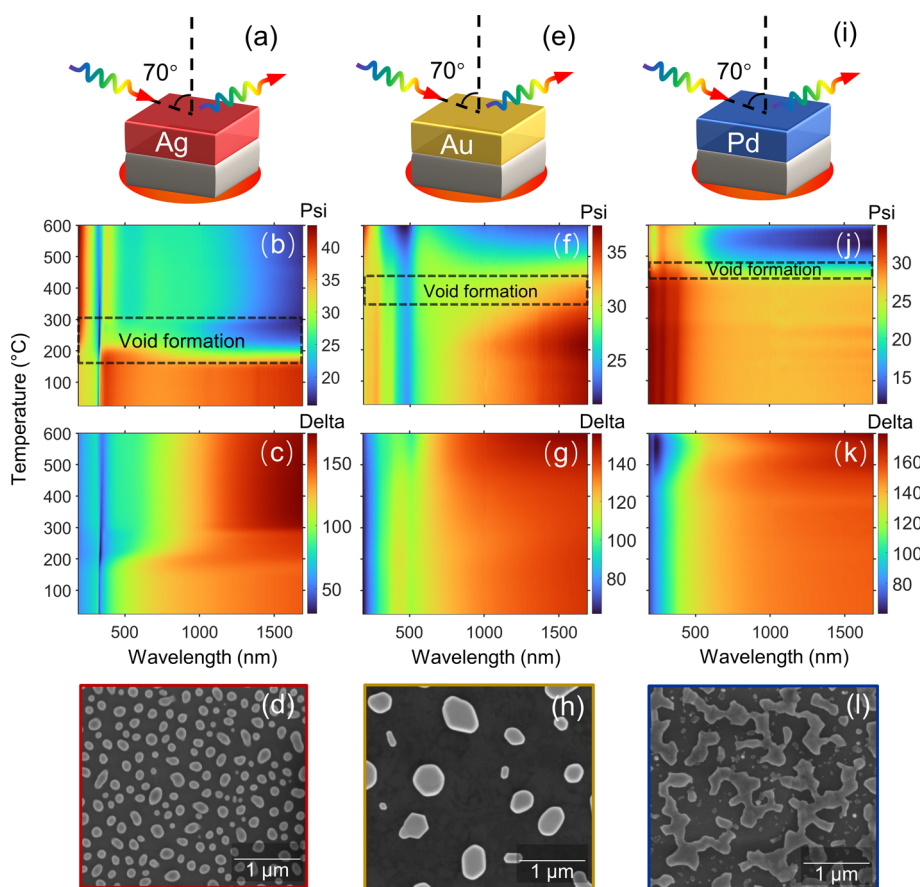
Figure 4. In situ optical characterization of pure metal nanoparticle formation. Schematic of the ellipsometry light path on the single metal (a) Ag, (e) Au, and (i) Pd thin film sample surfaces at 70°. Measured in situ (b, f, j) psi and (c, g, k) delta maps while the thin metal films ramping up from room temperature (25 °C) to 600 °C at 30 °C/min. Each pixel represents measurement at every 10 °C and 2 nm. The dashed boxes indicate the temperature range where the major void formation occurs. The colors refer to the measured values at each wavelength and temperature. (d, h, l) Corresponding SEM images of each nanostructure sample after the full 2 h annealing cycle to room temperature.

can also form fully alloyed nanoparticles with annealing at 500 °C.[37] Note that while the melting temperatures of bulk Au, Ag, and Pd are documented in the literature (1064, 961, and 1,555 °C,[43] respectively), the melting points of the thin films can be lower than their bulk counterparts due to size effects and the interactions with the substrate. Thus, at 600 °C, the significant changes in morphology occur without the onset of melting, critical for the SSD process interrogate here. As depicted in Figure 4a,e,i, the ellipsometer chamber is designed with two fused silica windows to allow the light source of the ellipsometer to project on the sample surface at a fixed incidence angle of 70°. This setup enables monitoring the real time amplitude ratio, psi (Ψ), and phase shift, delta (Δ), of the reflected s- and p-polarized signal to characterize the reflection behavior[50] during the dewetting process.

The in situ psi and delta spectra convey the temperature-induced changes in Figure 4. At room temperature (25 °C), the SE spectra of Ag and Au in Figure 4b,c,f,g have a sharp reflection dip around 325 nm (~3.8 eV) and 490 nm (~2.5 eV), in good agreement with our band structure calculations for interband transitions in Figure 2. However, the optical transition for Pd is absent here due to a much lower transition energy needed in the mid-infrared region. SE temperature maps reveal unique in situ optical behaviors among the three single metal thin film samples. For instance, the SE spectra of Ag are mostly unchanged and start to deviate when heated to

200 °C due to potential void formation. More drastic changes occur during the temperature range of 200−300 °C (about 25% decrease in psi intensity), correlating with the growth of voids to interconnected worm-like nanostructures and irregular nanoislands. After reaching the critical temperature of 300 °C, these nanoislands favor reshaping into domes (spherical caps) to minimize the system's free energy due to Rayleigh-like instabilities.[23] Similar void propagation and growth are also observed in the ex situ SEM micrographs of Ag dewetting process reported elsewhere.[33,49] Minor differences of the SE spectra between the first minute and 1 h while holding at 600 °C (see Figure S6) suggest that the temperature is sufficient for the Ag system to reach its equilibrium state with well-defined nanoparticle shapes and sizes. An SEM plan-view image of the nanoparticles after cooling is presented in Figure 4d. These dome-shaped nanoparticles have a nonuniform distribution with an average height of 55.3 ± 14.1 nm, diameter of 158.2 ± 55.7 nm, aspect ratio of 0.83 ± 0.14, and coverage area of 37.6% (see Figure S7 and Table S3).

Contrary to the behavior of Ag, the Au thin film shows very modest dewetting process below 350 °C, as seen in Figure 4f,g, where it maintains its two major reflection dips around 330 and 490 nm (corresponding to interband transitions at 4.0 and 2.5 eV, respectively).[34] Upon heating, a large portion of voids begin to form and grow, causing the reflection dip in the UV region to vanish. Comparing the SE spectra at the beginning
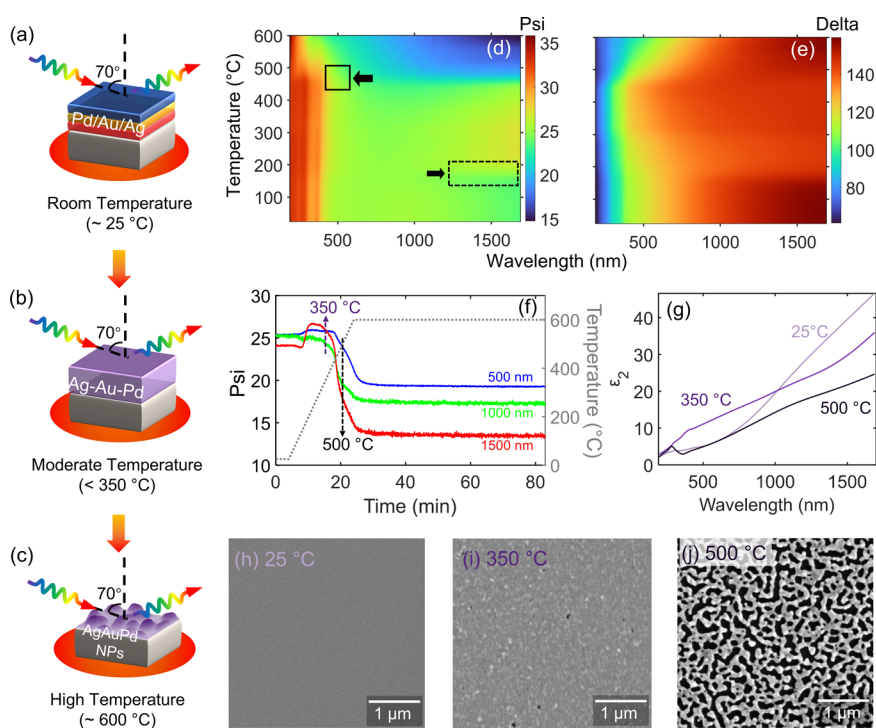
Figure 5. In situ analysis of AgAuPd nanoparticle formation. Schematic of the light path on the surface of (a) as deposited trilayer thin film stack, Pd/Au/Ag (from top to bottom), at room temperature, (b) interdiffused thin film at moderate temperature, and (c) post-annealed ternary alloy, AgAuPd, nanoparticles (NP) at high temperature at 70°. In situ (d) psi and (e) delta maps measured by an ellipsometer during sample annealing treatment from room temperature (RT, 25 °C) to 600 °C. Each pixel represents a measurement at every 10 °C and 2 nm. The color scale refers to the measured values at each wavelength and temperature. The black dashed and solid boxes display the first drastic change observed for NIR (1200−1690 nm) and vis (440−580 nm), respectively. (f) Dynamic trajectory of measured psi at wavelength of 500 (blue), 1000 (green), and 1500 nm (red) and temperature changes (gray) every 3 s during the annealing. The purple and black dashed arrows indicate the temperature at 350 and 500 °C, respectively. (g) Fitted dielectric functions ε_1 and ε_2 for the top layer above the substrate and corresponding SEM micrograph at (h) 25 °C, (i) 350 °C, and (j) 500 °C (detailed fitting models, see Figure S10).

and the end of the holding at 600 °C, the changes indicate the Au nanoparticles are still undergoing further morphological evolution within 1 h, which differs from the Ag case (see Figure S6d and Figure 6e). The shape and size of the annealed Au samples in Figure 4h mostly consist of faceted nanoparticles[51] (average height: 97.3 ± 32.6 nm, average diameter: 398.9 ± 141.9 nm, average aspect ratio: 0.85 ± 0.08) with a smaller coverage of 31.7% (see Figure S8 and Table S4).

In contrast, the dewetting mechanism has not been initiated for Pd until 450 °C; therefore, there is almost no change for the SE spectra in Figure 4j,k. The voids start to form later and cause a major dip at 220 nm. Further heating at 600 °C for a longer time provides more energy to the system, facilitating void growth and the formation of irregular nanoislands, as seen from the SEM image in Figure 4l. We have also tracked the in situ SE measurements during the cooling down process (see Figure S9) and found minute differences, which verify that the nanostructures characterized by the ex situ SEM after the annealing process are close to the ones at the final stage of the heating. Our findings clarify that the annealing approach of holding the sample at 600 °C for 1 h facilitates the formation of well-defined nanoparticles for both Ag and Au, whereas Pd may need a further annealing treatment at higher temperature or longer processing times.[52] Although the final products vary depending on the composition, initial film thickness, deposition conditions, and annealing conditions (temperature, atmosphere, and time),[43] this surface diffusion process, including void formation and growth and the evolution of

nanoislands during dewetting, alters morphology and also leads to a corresponding change in optical performance from thin film to nanoparticles.

In Situ Optical Characterization of Ternary AgAuPd Thin Film. Compared to the monometallic system above, the SSD process for the AgAuPd ternary alloy is strongly affected by interdiffusion of different elements, and the order in which the metals are deposited (due to surface diffusion between first metal deposited and the substrate).[35,53] The transition from the schematics in Figure 5a−c shows the leading mechanism from the initial trilayer stack to the formation of an intermixed (interdiffused) alloyed layer at an early stage, followed by void formation and growth to the eventual development of fully alloyed nanoparticles as temperature increases during the dewetting process. Unlike the single metal system, the in situ SE spectra in Figure 5d,e of the ternary system do not show similar optical changes across all wavelengths. Reflection measurements in the NIR start to increase around 180 °C and then sharply drop at 420 °C, while features at vis (500 nm) are well maintained until 450 °C. These distinctive optical signatures are tracked at three representative wavelengths, 500, 1000, and 1500 nm, for every 3 s (1.5 °C for temperature change) instead of every 5 °C over the annealing cycle in Figure 5f. Through quantitative comparison, it is evident that the dynamic trajectories of the three wavelengths shift gradually from 120 °C and undergo more drastic change after 400 °C until the thermal stabilization at high temperatures (600 °C). In this case, longer wavelengths exhibit
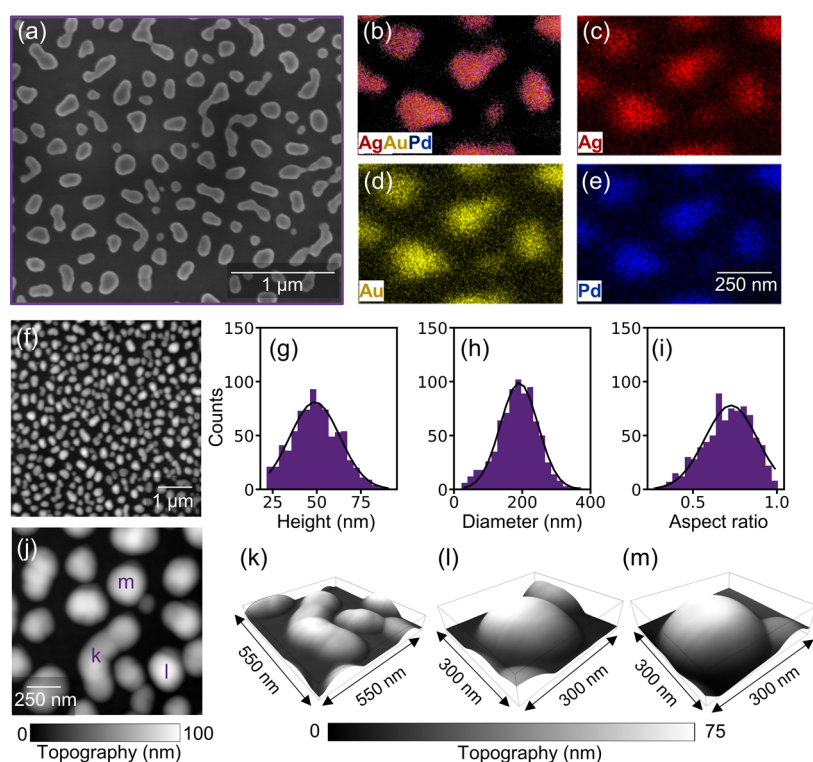
Figure 6. Fully alloyed AgAuPd nanoparticles. (a) SEM overview of the post-annealed ternary alloy AgAuPd nanoparticles. (b−e) EDS composition maps of several representative nanoparticles with an atomic concentration analysis of Ag:Au:Pd = 34:32:34 (see Figure S13 and Table S5). (f) AFM morphology scan and dimension statistics with (g) an average height of 48 ± 12 nm, (h) average diameter of 158 ± 55 nm, and (i) average aspect ratio of 0.78 ± 0.1 (detailed analysis, see Figure S14 and Table S6). Solid lines refer to the Gaussian fits. (j) AFM top-view scan and (k−m) 3D AFM images of representative AgAuPd nanoparticles. The color scales refer to topography.

greater sensitivity, with a 70% decrease in intensity at 1000 nm from 400 to 600 °C, suggesting susceptibility to potential changes induced by increasing roughness and void formation.[54,55] To identify the reason for the drastic changes occurring around 400 °C, we replicate the sample annealing process without holding time at two critical temperatures, 350 and 500 °C, to establish a solid relationship between optical changes and compositional/morphological changes induced by SSD. The macroscopic optical characterization is analyzed by multiangle SE measurements using the B-spline model to fit the dielectric functions of the topmost layer in Figure S10, comprising both metal nanostructures and air, while the optical properties and thickness of the bottom Si substrate and its native oxide layer are fixed, as suggested by the literature.[33,56] Figure 5g shows that an absorption peak emerges at 285 nm as the sample achieved 500 °C. The SEM micrographs in Figure 5h−j reveal that most voids start appearing around 350 °C and grow into the interconnected nanostructures up to 500 °C. Complementary X-ray photoelectron spectroscopy (XPS, see Figure S11) helps to confirm the intermediate interdiffusion stage with a larger portion of Ag and Au detected on the 350 °C surface compared to the as-deposited trilayer stack, which is a good indication of an alloyed thin film. Hence, it is conclusive that the initial and subsequent optical changes between 120 and 400 °C are directly attributed to the intermixing between Ag, Au, and Pd layers with higher roughness, while the significant changes after 400 °C entail plasmonic behavior excited by the growth of metal nanostructures. This finding agrees with the consensus of how SSD generally occurs in ternary systems, where the dominant mechanism at moderate temperatures is interdiffu-

sion of the metal atoms, and nanoisland formation is prioritized at a later high-temperature stage.

Chemical and Morphological Analyses of Post-annealing AgAuPd Nanoparticles. The SEM image in Figure 6a shows that the dewetting process of Ag−Au−Pd is nearly completed, with the formation of dome-shaped AgAuPd nanoparticles, similar to those observed in Ag and Au, albeit with a few irregular-elongated nanoparticles present in the system, after holding at 600 °C for 1 h (a consequence of coalescence). We confirm the uniform distribution of each metal across the nanoparticles, rather than any potential core−shell structure, by performing energy-dispersive X-ray spectroscopy (EDS) elemental mapping in Figure 6b−e. The average chemical composition of the nanoparticles is 34:32:34 AgAuPd (Figure S13 and Table S5). In addition, the AFM scan and statistics in Figure 6f−i present an average height of 49.7 ± 13.2 nm and an average diameter of 185.9 ± 58.4 nm (for a detailed analysis, see Figure S14 and Table S6). In particular, the average aspect ratio is calculated to be 0.71 ± 0.14, indicating the presence of irregular nanoislands where the length and width of each nanoparticle site has a nonunity aspect ratio.

Figure 6j and Figure S15 illustrate the presence of both individual domes and coalesced nanoislands on the sample surface. The AFM 3D images depicted in Figure 6k,m confirm that elongated islands result from the coalescence of smaller nanoparticles, hinting at potential further growth (see also Figure 6m for an incomplete ripening situation). Conversely, Figure 6l shows a solitary, isolated, dome-shaped nanoparticle. To compare the effect of metal deposition sequence on the overall SSD process, we also fabricate and anneal a 15 nm Pd/
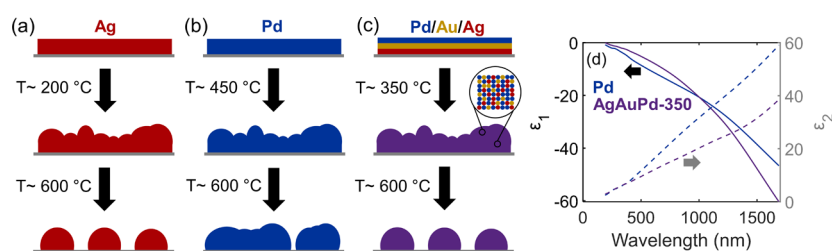
Figure 7. SSD dewetting process in metallic alloys. Schematic of SSD dewetting process for (a) Ag, (b) Pd, and (c) Pd/Au/Ag on a Si substrate. The inset shows the interdiffusion between different layers. (d) Dielectric functions ε_1 (solid line) and ε_2 (dashed line) of 15 nm Pd film and AgAuPd (annealed at 350 °C). The corresponding colors represent Ag in red, Pd in blue, Au in gold, and AgAuPd in purple.
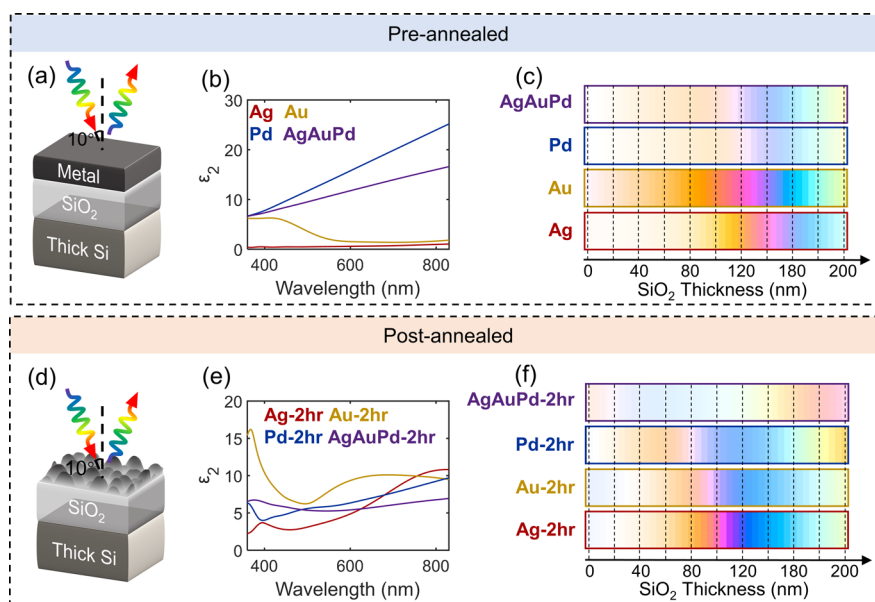

Figure 8. Color filters through dewetting. Pre-annealed: (a) Schematic of the multilayer device consisting of a 15 nm thin metal film and a SiO_2 layer with varying thickness on Si substrate. (b) Imaginary dielectric function ε_2 of pure metal thin film, Ag, Au, Pd, and multilayer Pd/Ag/Au thin film. (c) Corresponding simulated reflective color pixels of the full device for different metal layers with 0−200 nm SiO_2 at 10°. Post-annealed: (d) Schematic of the multilayer device with nanoparticles on the top and unchanged SiO_2 after the full 2 h annealing cycle. (e) Fitted dielectric function ε_2 of Ag, Au, and Pd and 1 h annealed AgAuPd layer with nanoparticles (detailed fitting, see Figure S19). (f) Simulated final reflective colors of the optical device.

Ag/Au thin film. Upon similar annealing conditions, this sample presents nanoparticles with a very asymmetric shape (see Figure S16), resulting from partially suppressed surface diffusion when compared to the dome-shaped islands from the Pd/Au/Ag film. Therefore, to enhance the dewetting process, we anneal another Pd/Au/Ag sample under the same controlled environment but with a longer holding time of 3 h at 600 °C. As expected, this sample exhibits similar chemical composition with a more uniform spatial and size distribution (average height: 47.5 ± 12.3 nm, average diameter: 158.1 ± 54.8 nm, average aspect ratio: 0.78 ± 0.14) while still maintaining the optical features in the wavelength of 250−400 nm range, compared to the 1 h annealed nanoparticles (see Figures S17 and S18 and Tables S7 and S8). Alternatively, higher temperatures (700−900 °C) can also help the system reach its equilibrium state, as priorly reported.[35] Hence, adding Ag and Au to Pd is a promising approach to help the ternary system achieve final nanoparticles with different optical properties from its pure constituents.

We summarize the experimental findings in Figure 7, with a qualitative model that describes the overall dewetting process within metallic alloys. Metals with low surface energy, such as Ag and Au, can initiate the SSD at moderate temperatures and form well-defined nanoparticles after a full annealing cycle at 600 °C for 1 h. In contrast, a high surface energy hinders the dewetting process of Pd, delaying void growth until 450 °C and resulting in only irregular interconnected nanoislands after the annealing cycle. Figure 7c shows that adding Ag and Au to Pd enables the interdiffusion between different layers at intermediate temperatures (∼350 °C), decreases the surface energy, and promotes the completion of SSD. Furthermore, the optical properties of the ternary alloy thin film formed at 350 °C are found to be close to those of pure Pd film, as shown in Figure 7d. This result aligns well with our initial DFT simulations, which revealed that the optical properties for the bulk ternary AgAuPd alloy are dominated by the transitions from Pd d states to Pd/Ag hybridized s states. Therefore, adding Ag and Au to Pd can facilitate the formation of nanoparticles via SSD while concomitantly maintaining the optical properties of Pd. In summary, alloying provides a useful pathway to control the formation of nanostructures with the Pd-like optical behavior.

Alloys for Color Filters. Motivated by the optical changes stemming from the transition from thin film to nanoparticle during the dewetting process, we identify it as a key factor for applications as irreversible color filters. Here, we propose a

multilayer reflective color filter perceived by human eyes based on a 15 nm thin metal film and a SiO_2 layer with varying thickness on a Si substrate, as shown in Figure 8. The top metal layer is selected from the four metallic materials tested, Ag, Au, Pd, and Pd/Ag/Au, with the imaginary dielectric function, ε_2 (see Figures 8b and 2). The thermally stable SiO_2 layer under 600 °C (with a melting point of ~1,411 °C[57]) plays a critical role in shifting the propagating light phase to generate vivid colors.[58] Also, a thickness of 200 nm does not hinder the heat transfer or alter the surface energy between the Si substrate and metal layer during dewetting because it already possesses a thin native oxide layer (SiO_2). In the pre-annealed state, the color filters consisting of the Au layer have the highest contrast, while colors of the Pd-based optical device appear more pastel with subtle gradients, according to RGB color simulations.

The multilayer device would then be annealed under a controlled environment, similar to the process undergone for all samples. After annealing, the top metal thin film layer completes the dewetting and forms nanostructures, following the schematic in Figure 8d. This topmost layer containing the nanoparticles has dielectric functions plotted in Figure 8e, as acquired from the dewetting experiments above. In contrast to their thin film stage, the post-annealed Ag and Au have higher absorption (ε_2) than Pd, owing to more scattering and plasmonic resonance (while most of features are in the UV range) excited by the rounded nanoparticles compared to the irregular interconnected nanoislands (for detailed fitting see Figure S19). Integrating the optical properties of this critical layer yields the final colors depicted in Figure 8f. A comparison of colors between pre- and post-annealed films demonstrates that the annealing step aids in fading the colors of devices employing Ag−Au−Pd and Au. Specifically, the limited color variations of the final ternary alloy device are imperceptible to human eyes. Conversely, the hues in Ag and Pd devices get more evident. Samples before and after the heating process with a SiO_2 thickness <5 nm on Si substrate with colors in Figure S20 matched well with the simulated color palette in Figure 8c,f. Our proof-of-concept work demonstrates that this system could achieve irreversible color tuning resulting from the efficient and low-cost dewetting process of the top layer from an initial thin film to the final nanoparticle state, which can be applied for color printing or data encryption.

■ CONCLUSIONS

In summary, we quantified the optical behavior of the AgAuPd ternary alloy across the macro- and nanoscale during the dewetting process, which transforms thin films into 3D metallic nanostructures. With this work, we addressed the previously underexplored real-time optical changes of the bulk AgAuPd model system from a fundamental solid-state physics perspective using DFT, discovering that its optical properties originate from the transition from Pd d states to Pd/Ag hybridized s states. We identified a unique feature in the IR range of the spectrum due to the proximity of the d band to the Fermi level. Experimentally, we implemented the scalable SSD process to fabricate arrays of pure and alloyed NPs by annealing single- and trilayer thin films. Simultaneously, our in situ optical and ex situ surface analyses unveiled the combined effects of chemical composition and morphology on optical behavior during the annealing process. In pure metal systems, optical evolution is primarily driven by morphological changes. However, for the AgAuPd alloy, it is initially influenced by

chemical composition at moderate temperatures, shifting toward morphological evolution from two-dimensional film to three-dimensional nanostructures at late stages. Our results stress the importance of surface diffusion, as well as inter- and intradiffusion to achieve nanostructures with dielectric functions not attained by pure metals. Note that the contribution of each pure metal in such complex systems is likely nonlinear, which, in turn, is a feature for novel optical materials. The expansion of our paradigm to polyelemental metallic nanostructures (with >7 metals) could be used to "fine-tune" spectrum control, very relevant for photocatalysis.

■ EXPERIMENTAL SECTION

Band Structure Calculations. To best represent the system without compromising the computational cost and time, a face centered cubic (fcc) supercell was employed with 27 sites, which corresponds to a $3 \times 3 \times 3$ replication of the primitive fcc cell. The distribution of the Ag, Au, and Pd atoms in the cell, in equal quantities, was optimized using the special quasi-random structures (SQS) method,[38] that is, the best periodic supercell approximations to the true disordered state for a given number of atoms per supercell, as implemented in the ATAT package.[59,60] A representation of the supercell is shown in Figure S1, and the corresponding atomic positions are shown in Table S1. The total-energy and electronic-structure calculations were obtained via density functional theory (DFT) as implemented in the SIESTA code.[61] Exchange and correlation are described within the Perdew−Burke−Ernzerhof functional[62] and a double ζ-polarized (DZP) basis-set with a real-space grid cutoff of 500 Ry. The BZ is sampled using a $9 \times 9 \times 9$, Monkhorst−Pack k-point mesh. We optimized the geometry of each individual component of the alloy in its corresponding primitive fcc cell, finding as cubic (primitive) lattice parameters 4.13(2.92), 4.10(2.90), and 3.97(2.81) Å for Ag, Au and Pd, respectively. For the $3 \times 3 \times 3$ superlattice, the optimized lattice is 12.27(8.67) Å. To unfold the supercell band structure, we applied the unfolding method as described in ref 63 and available in the SIESTA package.

Sample Fabrication. All pure metal thin films were fabricated by the e-beam evaporation of single metals with a deposition rate of ~1.5 Å/s with a chamber pressure of 3.5×10^{-6} Torr at room temperature (CHA E-Beam Evaporator at the Center for Nano-Micro Manufacturing, CNM2, at UC Davis). The trilayer stack was deposited from Ag (99.99%), Au (99.99%), and Pd (99.95%, from Kurt J. Lesker Company) with the same thickness of ~5 nm, from bottom to top, sequentially. The sample stage was rotated at 6 rpm during the deposition. The thin films were deposited onto 1×1 cm² n-doped Si substrates, which were cleaned with 2-propanol and deionized water and then dried with N_2 gas at the preparation stage.

Thin Film Dielectric Functions and Thickness Characterizations. The ellipsometry measurements, psi and delta, were acquired on the J.A. Woollam VASE ellipsometer in CNM2 at UC Davis, at 55, 65, and 75° in the wavelength of 193−1680 nm. These measurements were then used to fit the optical model (General Oscillators), which includes the dielectric functions and film thickness of the sample on the software, CompleteEASE. The beam spot size is 3×12 mm when measured at 75°.

In Situ Ellipsometry. The samples were transferred to the Linkam RC-2 heating stage (maximum temperature: 600 °C) equipped with a J.A. Woollam VASE ellipsometer in CNM2 at UC Davis. The heating stage was able to heat the samples from room temperature (25 °C) to 600 °C with a ramping rate of 30 °C/min, hold at 600 °C for 1 or 3 h to allow the sample to thermalize, and finally cool down to room temperature at 30 °C/min, the same rate as ramping up. Notice that the cooling rate was slower when the temperature is lower than 100 °C due to instrumental limitations. The sample chamber had two glass windows to let the reflection be measured at 70° and kept in a constant flow of Ar at 1 atm to prevent potential oxidation. The in situ measurements were taken every ~3 s during the process and analyzed

with B-spline models on CompleteEASE for real-time optical properties.

Scanning Electron Microscopy and Chemical Composition Analysis. The high-resolution electron micrographs of the samples were taken in the FEI Scios Dual Beam system equipped with an EDS detector (in CNM2 at UC Davis) with an accelerating voltage of 5 kV and current of 0.1 nA. The surface energy-dispersive X-ray spectroscopy (EDS) was operated with a 10 kV accelerating voltage and 2 nA current.

Atomic Force Microscopy. Topography measurements were carried out with MFP-3D model AFM by Asylum Research (Oxford Instruments) with an AC tapping mode in air. The AC160TS-R3 probe with a force constant of 26 N/m and resonance frequency of 300 kHz was used.

Color Simulation. The color pixels (RGB coordinates) were simulated by the color calculation function provided on CompleteEASE based on the transfer matrix method (TMM) with an angle of incidence (AOI) at 0°, standard observer of 10° (1964), and illuminant of D65. The models were based on a top metasurface layer (dielectric functions found from our samples) and an optically thick Si substrate sandwiched between a middle SiO_2 layer with varied thickness from 0 to 200 nm with an increment of 5 nm.

■ ASSOCIATED CONTENT

⑤ⓘ Supporting Information

The Supporting Information is available free of charge at https://pubs.acs.org/doi/10.1021/acsami.4c11397.

> Representation of the fcc supercell used to simulate the alloy by DFT, sample thickness and dielectric function fittings characterized by ellipsometry, AFM and SEM of pre- and post-annealed (1 h, 3 h) samples, temperature profile for the annealing cycle, in situ ellipsometry measurements while heating samples up to 600 °C and down to 25 °C, ex situ surface chemistry analysis (EDS, XPS), reflection measurements for pre-annealed thin film and post-annealed nanostructures (PDF)

■ AUTHOR INFORMATION

Corresponding Author

Marina S. Leite — *Department of Materials Science and Engineering, University of California - Davis, Davis, California 95616, United States;* ⓘ orcid.org/0000-0003-4888-8195; Email: mleite@ucdavis.edu

Authors

Peifen Lyu — *Department of Materials Science and Engineering, University of California - Davis, Davis, California 95616, United States;* ⓘ orcid.org/0000-0001-7412-782X

Filipe Matusalem — *Instituto de Física Teórica, São Paulo State University (UNESP), São Paulo 01140-170, Brazil; Instituto Tecnológico de Aeronáutica (ITA), São José dos Campos 12228-900, Brazil;* ⓘ orcid.org/0000-0002-5305-9693

Ece Deniz — *Department of Materials Science and Engineering, University of California - Davis, Davis, California 95616, United States;* ⓘ orcid.org/0000-0001-6897-4416

Alexandre Reily Rocha — *Instituto de Física Teórica, São Paulo State University (UNESP), São Paulo 01140-170, Brazil;* ⓘ orcid.org/0000-0001-8874-6947

Complete contact information is available at:
https://pubs.acs.org/10.1021/acsami.4c11397

Author Contributions

M.S.L. conceived the idea of and supervised the project. A.R.R. led the DFT component of the work. P.L. fabricated the samples and performed their optical, morphological, and chemical characterizations, optical calculations, and data analysis. F.M. performed the DFT calculations. E.D. performed AFM and XPS measurements. The manuscript was written through contributions of all authors.

Notes

The authors declare no competing financial interest.

■ ACKNOWLEDGMENTS

■ REFERENCES

(1) Albrecht, G.; Ubl, M.; Kaiser, S.; Giessen, H.; Hentschel, M. Comprehensive Study of Plasmonic Materials in the Visible and Near-Infrared: Linear, Refractory, and Nonlinear Optical Properties. *ACS Photonics* **2018**, *5* (3), 1058−1067.

(2) Kadkhodazadeh, S.; Nugroho, F. A. A.; Langhammer, C.; Beleggia, M.; Wagner, J. B. Optical Property−Composition Correlation in Noble Metal Alloy Nanoparticles Studied with EELS. *ACS Photonics* **2019**, *6* (3), 779−786.

(3) Kravets, V. G.; Kabashin, A. V.; Barnes, W. L.; Grigorenko, A. N. Plasmonic Surface Lattice Resonances: A Review of Properties and Applications. *Chem. Rev.* **2018**, *118* (12), 5912−5951.

(4) Nishijima, Y.; Balčytis, A.; Naganuma, S.; Seniutinas, G.; Juodkazis, S. Tailoring Metal and Insulator Contributions in Plasmonic Perfect Absorber Metasurfaces. *ACS Appl. Nano Mater.* **2018**, *1* (7), 3557−3564.

(5) Tiburski, C.; Langhammer, C. Engineering Optical Absorption in Late Transition-Metal Nanoparticles by Alloying. *ACS Photonics* **2023**, *10* (1), 253−264.

(6) Gong, T.; Lyu, P.; Palm, K. J.; Memarzadeh, S.; Munday, J. N.; Leite, M. S. Emergent Opportunities with Metallic Alloys: From Material Design to Optical Devices. *Adv. Opt. Mater.* **2020**, *8* (23), 2001082.

(7) Hashimoto, Y.; Seniutinas, G.; Balčytis, A.; Juodkazis, S.; Nishijima, Y. Au-Ag-Cu nano-alloys: tailoring of permittivity. *Sci. Rep.* **2016**, *6* (1), 25010.

(8) Wang, J.; Zhang, P.; Xiahou, Y.; Wang, D.; Xia, H.; Möhwald, H. Simple Synthesis of Au−Pd Alloy Nanowire Networks as Macro-

scopic, Flexible Electrocatalysts with Excellent Performance. *ACS Appl. Mater. Interfaces* **2018**, *10* (1), 602−613.

(9) Peng, H.; Li, R.; Hu, J.; Deng, W.; Pan, F. Core−Shell Sn−Ni−Cu-Alloy@Carbon Nanorods to Array as Three-Dimensional Anode by Nanoelectrodeposition for High-Performance Lithium Ion Batteries. *ACS Appl. Mater. Interfaces* **2016**, *8* (19), 12221−12227.

(10) Jiang, W.; Low, B. Q. L.; Long, R.; Low, J.; Loh, H.; Tang, K. Y.; Chai, C. H. T.; Zhu, H.; Zhu, H.; Li, Z.; Loh, X. J.; Xiong, Y.; Ye, E. Active Site Engineering on Plasmonic Nanostructures for Efficient Photocatalysis. *ACS Nano* **2023**, *17* (5), 4193−4229.

(11) Swearer, D. F.; Zhao, H.; Zhou, L.; Zhang, C.; Robatjazi, H.; Martirez, J. M. P.; Krauter, C. M.; Yazdi, S.; McClain, M. J.; Ringe, E.; Carter, E. A.; Nordlander, P.; Halas, N. J. Heterometallic antenna−reactor complexes for photocatalysis. *Proc. Natl. Acad. Sci. U. S. A.* **2016**, *113* (32), 8916−8920.

(12) Parashar, P. K.; Komarala, V. K. Engineered optical properties of silver-aluminum alloy nanoparticles embedded in SiON matrix for maximizing light confinement in plasmonic silicon solar cells. *Sci. Rep.* **2017**, *7* (1), 12520.

(13) Zarick, H. F.; Erwin, W. R.; Boulesbaa, A.; Hurd, O. K.; Webb, J. A.; Puretzky, A. A.; Geohegan, D. B.; Bardhan, R. Improving Light Harvesting in Dye-Sensitized Solar Cells Using Hybrid Bimetallic Nanostructures. *ACS Photonics* **2016**, *3* (3), 385−394.

(14) Nugroho, F. A. A.; Darmadi, I.; Cusinato, L.; Susarrey-Arce, A.; Schreuders, H.; Bannenberg, L. J.; da Silva Fanta, A. B.; Kadkhodazadeh, S.; Wagner, J. B.; Antosiewicz, T. J.; Hellman, A.; Zhdanov, V. P.; Dam, B.; Langhammer, C. Metal−polymer hybrid nanomaterials for plasmonic ultrafast hydrogen detection. *Nat. Mater.* **2019**, *18* (5), 489−495.

(15) Deng, X.; Li, L.; Enomoto, M.; Kawano, Y. Continuously Frequency-Tuneable Plasmonic Structures for Terahertz Bio-sensing and Spectroscopy. *Sci. Rep.* **2019**, *9* (1), 3498.

(16) Ambardar, S.; Nguyen, D.; Binder, G.; Withers, Z. W.; Voronine, D. V. Quantum Leap from Gold and Silver to Aluminum Nanoplasmonics for Enhanced Biomedical Applications. *Appl. Sci.* **2020**, *10* (12), 4210.

(17) Andersson, C.; Serebrennikova, O.; Tiburski, C.; Alekseeva, S.; Fritzsche, J.; Langhammer, C. A Microshutter for the Nanofabrication of Plasmonic Metal Alloys with Single Nanoparticle Composition Control. *ACS Nano* **2023**, *17* (16), 15978−15988.

(18) Huynh, K.-H.; Pham, X.-H.; Kim, J.; Lee, S. H.; Chang, H.; Rho, W.-Y.; Jun, B.-H. Synthesis, Properties, and Biological Applications of Metallic Alloy Nanoparticles. *Int. J. Mol. Sci.* **2020**, *21* (14), 5174.

(19) Albrecht, W.; Bladt, E.; Vanrompay, H.; Smith, J. D.; Skrabalak, S. E.; Bals, S. Thermal Stability of Gold/Palladium Octopods Studied in Situ in 3D: Understanding Design Rules for Thermally Stable Metal Nanoparticles. *ACS Nano* **2019**, *13* (6), 6522−6530.

(20) Bueno, S. L. A.; Leonardi, A.; Kar, N.; Chatterjee, K.; Zhan, X.; Chen, C.; Wang, Z.; Engel, M.; Fung, V.; Skrabalak, S. E. Quinary, Senary, and Septenary High Entropy Alloy Nanoparticle Catalysts from Core@Shell Nanoparticles and the Significance of Intraparticle Heterogeneity. *ACS Nano* **2022**, *16* (11), 18873−18885.

(21) Zhang, S.; Wang, B.; Jiang, J.; Wu, K.; Guo, C. F.; Wu, Z. High-Fidelity Conformal Printing of 3D Liquid Alloy Circuits for Soft Electronics. *ACS Appl. Mater. Interfaces* **2019**, *11* (7), 7148−7156.

(22) McClure, J. P.; Boltersdorf, J.; Baker, D. R.; Farinha, T. G.; Dzuricky, N.; Villegas, C. E. P.; Rocha, A. R.; Leite, M. S. Structure−Property-Performance Relationship of Ultrathin Pd−Au Alloy Catalyst Layers for Low-Temperature Ethanol Oxidation in Alkaline Media. *ACS Appl. Mater. Interfaces* **2019**, *11* (28), 24919−24932.

(23) Ye, J.; Zuev, D.; Makarov, S. Dewetting mechanisms and their exploitation for the large-scale fabrication of advanced nanophotonic systems. *Int. Mater. Rev.* **2019**, *64* (8), 439−477.

(24) Gong, C.; Dias, M. R. S.; Wessler, G. C.; Taillon, J. A.; Salamanca-Riba, L. G.; Leite, M. S. Near-Field Optical Properties of Fully Alloyed Noble Metal Nanoparticles. *Adv. Opt. Mater.* **2017**, *5* (1), 1600568.

(25) Cencillo-Abad, P.; Franklin, D.; Mastranzo-Ortega, P.; Sanchez-Mondragon, J.; Chanda, D. Ultralight plasmonic structural color paint. *Sci. Adv.* **2023**, *9* (10), No. eadf7207.

(26) Mao, P.; Liu, C.; Song, F.; Han, M.; Maier, S. A.; Zhang, S. Manipulating disordered plasmonic systems by external cavity with transition from broadband absorption to reconfigurable reflection. *Nat. Commun.* **2020**, *11* (1), 1538.

(27) Yu, R.; Mazumder, P.; Borrelli, N. F.; Carrilero, A.; Ghosh, D. S.; Maniyara, R. A.; Baker, D.; García de Abajo, F. J.; Pruneri, V. Structural Coloring of Glass Using Dewetted Nanoparticles and Ultrathin Films of Metals. *ACS Photonics* **2016**, *3* (7), 1194−1201.

(28) Coppens, Z. J.; Kravchenko, I. I.; Valentine, J. G. Lithography-Free Large-Area Metamaterials for Stable Thermophotovoltaic Energy Conversion. *Adv. Opt. Mater.* **2016**, *4* (5), 671−676.

(29) Ko, J. H.; Kim, S. H.; Kim, M. S.; Heo, S.-Y.; Yoo, Y. J.; Kim, Y. J.; Lee, H.; Song, Y. M. Lithography-Free, Large-Area Spatially Segmented Disordered Structure for Light Harvesting in Photovoltaic Modules. *ACS Appl. Mater. Interfaces* **2022**, *14* (39), 44419−44428.

(30) Haechler, I.; Ferru, N.; Schnoering, G.; Mitridis, E.; Schutzius, T. M.; Poulikakos, D. Transparent sunlight-activated antifogging metamaterials. *Nat. Nanotechnol.* **2023**, *18* (2), 137−144.

(31) Worsch, C.; Kracker, M.; Edelmann, J.; Schubert, A.; Rüssel, C. Microfluidic plasmon sensors prepared by dewetting of metal films during hot-embossing of glass. *Sens. Actuators, B* **2014**, *202*, 365−372.

(32) Liao, T.-Y.; Lee, B.-Y.; Lee, C.-W.; Wei, P.-K. Large-area Raman enhancement substrates using spontaneous dewetting of gold films and silver nanoparticles deposition. *Sens. Actuators, B* **2011**, *156* (1), 245−250.

(33) Jacquet, P.; Kildemo, M.; Teisseire, J.; Gozhyk, I.; Jupille, J.; Lazzari, R. Monitoring silver solid-state dewetting with in situ ellipsometry. *Appl. Surf. Sci.* **2017**, *421*, 553−556.

(34) Magnozzi, M.; Bisio, F.; Canepa, M. Solid-state dewetting of thin Au films studied with real-time, in situ spectroscopic ellipsometry. *Appl. Surf. Sci.* **2017**, *421*, 651−655.

(35) Pandey, P.; Kunwar, S.; Sui, M.; Bastola, S.; Lee, J. Modulation of Morphology and Optical Property of Multi-Metallic PdAuAg and PdAg Alloy Nanostructures. *Nanoscale Res. Lett.* **2018**, *13* (1), 151.

(36) Li, S.-j.; Ping, Y.; Yan, J.-M.; Wang, H.-L.; Wu, M.; Jiang, Q. Facile synthesis of AgAuPd/graphene with high performance for hydrogen generation from formic acid. *J. Mater. Chem. A* **2015**, *3* (28), 14535−14538.

(37) Nugroho, F. A. A.; Iandolo, B.; Wagner, J. B.; Langhammer, C. Bottom-Up Nanofabrication of Supported Noble Metal Alloy Nanoparticle Arrays for Plasmonics. *ACS Nano* **2016**, *10* (2), 2871−2879.

(38) Zunger, A.; Wei, S. H.; Ferreira, L. G.; Bernard, J. E. Special quasirandom structures. *Phys. Rev. Lett.* **1990**, *65* (3), 353−356.

(39) Villegas, C. E. P.; Leite, M. S.; Marini, A.; Rocha, A. R. Efficient hot-carrier dynamics in near-infrared photocatalytic metals. *Phys. Rev. B* **2022**, *105* (16), No. 165109.

(40) Gong, C.; Kaplan, A.; Benson, Z. A.; Baker, D. R.; McClure, J. P.; Rocha, A. R.; Leite, M. S. Band Structure Engineering by Alloying for Photonics. *Adv. Opt. Mater.* **2018**, *6* (17), 1800218.

(41) Krayer, L. J.; Palm, K. J.; Gong, C.; Torres, A.; Villegas, C. E. P.; Rocha, A. R.; Leite, M. S.; Munday, J. N. Enhanced near-infrared photoresponse from nanoscale AgAu alloyed films. *ACS Photonics* **2020**, *7*, 1689.

(42) Johs, B.; Hale, J. S. Dielectric function representation by B-splines. *Phys. Status Solidi A* **2008**, *205* (4), 715−719.

(43) Thompson, C. V. Solid-State Dewetting of Thin Films. *Annu. Rev. Mater. Res.* **2012**, *42* (1), 399−434.

(44) Nanda, K. K.; Sahu, S. N.; Behera, S. N. Liquid-drop model for the size-dependent melting of low-dimensional systems. *Phys. Rev. A* **2002**, *66* (1), No. 013208.

(45) Hövel, M.; Gompf, B.; Dressel, M. Dielectric properties of ultrathin metal films around the percolation threshold. *Phys. Rev. B* **2010**, *81* (3), No. 035402.

(46) Abadias, G.; Simonot, L.; Colin, J. J.; Michel, A.; Camelio, S.; Babonneau, D. Volmer-Weber growth stages of polycrystalline metal

films probed by in situ and real-time optical diagnostics. *Appl. Phys. Lett.* **2015**, *107*, 183105.

(47) Galinski, H.; Ryll, T.; Elser, P.; Rupp, J. L. M.; Bieberle-Hütter, A.; Gauckler, L. J. Agglomeration of Pt thin films on dielectric substrates. *Phys. Rev. B* **2010**, *82* (23), No. 235415.

(48) Leroy, F.; Borowik, Ł.; Cheynis, F.; Almadori, Y.; Curiotto, S.; Trautmann, M.; Barbé, J. C.; Müller, P. How to control solid state dewetting: A short review. *Surf. Sci. Rep.* **2016**, *71* (2), 391−409.

(49) Quan, J.; Zhang, J.; Qi, X.; Li, J.; Wang, N.; Zhu, Y. A study on the correlation between the dewetting temperature of Ag film and SERS intensity. *Sci. Rep.* **2017**, *7* (1), 14771.

(50) Jellison, G. E. Data analysis for spectroscopic ellipsometry. *Thin Solid Films* **1993**, *234* (1), 416−422.

(51) Müller, C. M.; Mornaghini, F. C. F.; Spolenak, R. Ordered arrays of faceted gold nanoparticles obtained by dewetting and nanosphere lithography. *Nanotechnology* **2008**, *19* (48), 485306.

(52) Lee, Y.; Koh, K.; Na, H.; Kim, K.; Kang, J.-J.; Kim, J. Lithography-Free Fabrication of Large Area Subwavelength Antireflection Structures Using Thermally Dewetted Pt/Pd Alloy Etch Mask. *Nanoscale Res. Lett.* **2009**, *4* (4), 364.

(53) Kunwar, S.; Pandey, P.; Sui, M.; Bastola, S.; Lee, J. Evolution of Ternary AuAgPd Nanoparticles by the Control of Temperature, Thickness, and Tri-Layer. *Metals* **2017**, *7* (11), 472.

(54) Raether, H. On the influence of roughness on the optical properties of surfaces: Plasma resonance emission and the plasmon dispersion relation. *Thin Solid Films* **1975**, *28* (1), 119−124.

(55) Invernizzi, C.; de Ferri, L.; Comite, V.; Fermo, P.; Malagodi, M.; Pojana, G. Correlation between surface roughness and spectral features in IR-reflection spectroscopy. *Microchem. J.* **2022**, *172*, No. 106874.

(56) Beyene, H. T.; Weber, J. W.; Verheijen, M. A.; van de Sanden, M. C. M.; Creatore, M. Real time in situ spectroscopic ellipsometry of the growth and plasmonic properties of au nanoparticles on SiO2. *Nano Res.* **2012**, *5* (8), 513−520.

(57) Gayler, M. L. V. Melting Point of High-Purity Silicon. *Nature* **1938**, *142* (3593), 478−478.

(58) Gong, T.; Lyu, P.; Leite, M. S. Scalable Superabsorbers and Color Filters Based on Earth-Abundant Materials. *ACS Appl. Opt. Mater.* **2023**, *1* (4), 825−831.

(59) van de Walle, A.; Asta, M.; Ceder, G. The alloy theoretic automated toolkit: A user guide. *Calphad* **2002**, *26* (4), 539−553.

(60) van de Walle, A.; Tiwary, P.; de Jong, M.; Olmsted, D. L.; Asta, M.; Dick, A.; Shin, D.; Wang, Y.; Chen, L. Q.; Liu, Z. K. Efficient stochastic generation of special quasirandom structures. *Calphad* **2013**, *42*, 13−18.

(61) Soler, J. M.; Artacho, E.; Gale, J. D.; García, A.; Junquera, J.; Ordejón, P.; Sánchez-Portal, D. The SIESTA method for ab initio order-N materials simulation. *J. Phys.: Condens.Matter* **2002**, *14* (11), 2745.

(62) Perdew, J. P.; Burke, K.; Ernzerhof, M. Generalized Gradient Approximation Made Simple. *Phys. Rev. Lett.* **1996**, *77* (18), 3865−3868.

(63) Mayo, S. G.; Yndurain, F.; Soler, J. M. Band unfolding made simple. *J. Phys.: Condens. Matter* **2020**, *32* (20), 205902.